JOURNAL OF APPLIED PHYSICS **105**, 053304 (2009)

# Terahertz laser modulation of electron beams

J. G. Neumann,[1,a)] R. B. Fiorito,[1] P. G. O'Shea,[1,b)] H. Loos,[2,c)] B. Sheehy,[2] Y. Shen,[2] and Z. Wu[2]
[1]*Institute for Research in Electronics and Applied Physics, University of Maryland, College Park, Maryland 20742, USA*
[2]*National Synchrotron Light Source, Brookhaven National Laboratory, Upton, New York 11973-5000, USA*

(Received 9 August 2008; accepted 18 December 2008; published online 4 March 2009)

The study of modulated electron beams is important because they can be used to produce coherent radiation, but the modulations can cause unwanted instabilities in some devices. Specifically, in a free electron laser, proper prebunching at the desired emission frequency can enhance performance, while bunching resulting from instabilities and bunch compression schemes can degrade performance. In a photoinjector accelerator, tailoring the shape of the drive laser pulse could be used as a technique to either enhance or mitigate the effect of these modulations. This work explores the possibility of creating deeply modulated electron beams at the photocathode by using a modified drive laser designed to produce multiple subpicosecond pulses repeated at terahertz frequencies. Longitudinal space charge forces can strongly influence the evolution of modulations by converting density modulations to energy modulations. Experiments at the Source Development Laboratory electron accelerator at Brookhaven National Laboratory and PARMELA simulations are employed to explore the dynamics of electron beams with varying charge and with varying initial modulation. Finally, terahertz light generated by a transition radiator is used to confirm the structure of the electron beam. © *2009 American Institute of Physics*. [DOI: 10.1063/1.3075563]

## I. INTRODUCTION

Modulated electron beams in particle accelerators can be produced by design or unintentionally. The modulation may be deliberately added when the generation of coherent radiation at the modulation frequency is desirable.[1,2] Conversely, it may be preferred to suppress unwanted modulation in cases where coherent synchrotron radiation (CSR) induced beam degradation is a concern.[3,4] In either case it is important to understand and control the evolution of longitudinal modulation in electron beams.

In electron photoinjectors, fluctuations in current resulting from the drive laser or space charge forces near the cathode can be amplified and/or converted to energy spread as the beam is accelerated.[5] During subsequent beam manipulation stages, such as injection bends or compression chicanes, these perturbations may result in coherent synchrotron radiation (CSR). Magnetic chicanes are often used to compress electron bunches thereby increasing the peak current and the free electron laser (FEL) gain. However, CSR increases in intensity as the bunch length decreases. CSR at long (terahertz) wavelengths can directly degrade FEL performance through two mechanisms: by direct degradation of the electron beam quality (current, emittance, and energy spread) and through generation of mirror heating and hence distortion that can limit high power FEL oscillator operation.[6] Similarly, the longitudinal space charge instability can amplify small oscillations in longitudinal beam density through space charge forces to create strongly distorted longitudinal phase space at the end of the accelerator.[7,8]

Several solutions have been proposed for smoothing small longitudinal electron beam modulations, including laser heating to increase the uncorrelated energy spread of the beam.[2] This allows for Landau damping which can prevent the development of instabilities while keeping the accelerated beam within tolerance for proper FEL operation. Another potential solution includes the smoothing of the incident drive laser pulse.[9] In this case, an acousto-optical programmable dispersive filter is used to create a smooth UV pulse profile. This method has produced a smoother electron beam in longitudinal phase space, with reduced transverse emittance, and matched slices over a larger part of the pulse. An additional study used a pulse stacker to confirm the suitability of such pulseshaping techniques (that is, confirming prompt emission of electrons at the cathode) for producing low emittance electron bunches.[10]

The work reported here focuses instead on deep current modulation imposed on the electron beam at the photocathode, specifically at terahertz frequencies, and on how such a bunch train propagates through a linear accelerator to relativistic energy. This modulation is imposed on the drive laser and is designed to produce multiple subpicosecond micropulses repeated at terahertz frequencies on the initial laser pulse. Similar studies have also been conducted at much lower energies; for example, the 10 keV University of Maryland electron ring was used to explore space charge dominated beam physics and employed a laser switch to generate gigahertz frequency density modulation on combined thermionic and photoemitted electron beams.[11–13] Short single

---

[a)] Present address: Naval Research Laboratory, Washington, DC 20375. Electronic mail: jonathan.neumann@nrl.navy.mil.

[b)] Also at Department of Electrical and Computer Engineering, University of Maryland.

[c)] Present address: Stanford Linear Accelerator, Menlo Park, CA 94025.

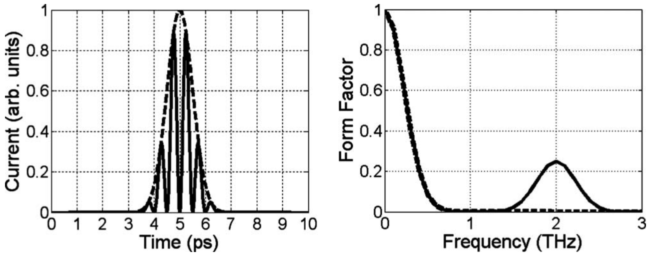

FIG. 1. (Left) Unmodulated (dashed) and modulated (solid) input beam profile. (Right) Calculated form factor for unmodulated (dashed) and modulated (solid) electron beams

bunch studies have also been conducted at the Source Development Laboratory (SDL) in order to generate intense single-cycle terahertz pulses.[14]

Deep longitudinal density modulation in an electron beam is an important condition for radiation in many devices, including klystrons, magnetrons, and free electron lasers. In general, the total radiation emitted by a group of particles from any mechanism can be described by Eq. (1),[15,16]

$$\frac{d^2W}{d\omega d\Omega} = \frac{d^2W_1}{d\omega d\Omega}[N_e + N_e(N_e - 1)f(\omega)], \tag{1}$$

where $d^2W_1/d\omega d\Omega$ is the energy emitted by one electron, $N_e$ is the number of electrons in the bunch, and $f(\omega)$ is the bunch form factor. The form factor $f(\omega)$ is related to the Fourier transform of the charge density and is given by[16,17]

$$f(\omega) = \left| \int d\vec{r} S(\vec{r}) e^{i(\omega/c)\hat{n}\cdot\vec{r}} \right|^2, \tag{2}$$

where $S(\vec{r})$ is the mean particle distribution of the beam normalized by the number of electrons, $\omega$ is the angular frequency of the emitted light, and $c$ is the speed of light. Often, Eq. (2) is separated into longitudinal and transverse components. In our analysis we assume that the transverse profile of the beam is Gaussian, and the longitudinal component of the form factor is evaluated numerically. Given this formulation, the amount of light produced by a modulated electron beam is a function of both the total bunch charge and the charge density modulation of the electron beam, as shown by Rosenzweig *et al.*[18] Figure 1 shows how the form factor of a smooth beam is affected when it becomes bunched. While the form factor is useful for calculating the amount of radiation that would be generated by the beam, it is also useful for characterizing the degree of beam bunching. Techniques for measuring electron beam bunch length using coherent transition radiation (CTR) relating to this form factor have been demonstrated by Rule *et al.*[19]

A beam with the profile shown in Fig. 1 could be used to generate radiation directly, such as in a transition radiator. Alternatively, this beam could be used as an input to a device such as a free electron laser, where the interaction between the electrons and radiated energy cases the beam to become more tightly bunched. Using such a prebunched beam is potentially quite beneficial in this case; the resonant wavelength can be excited without a drive signal and the radiation can grow faster than exponential.[20] Coupling the prebunching mechanism at the cathode with a short wiggler could yield a compact accelerator-based high power terahertz source, but the space charge forces near the gun may cause debunching prior to reaching the wiggler, making it impossible to quickly realize saturation. To assess the severity of the problem in a simple way, the plasma frequency of the beam using the longitudinal relativistic mass is considered,[21]

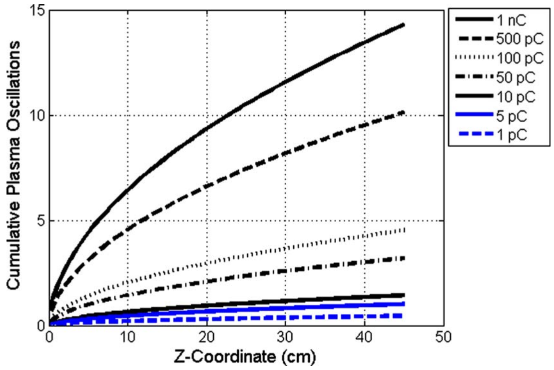

FIG. 2. (Color online) Cumulative plasma oscillations through acceleration to 38 MeV as a function of $z$-coordinate and total charge.

$$\omega_p = \sqrt{\frac{q^2 n}{\varepsilon_0 \gamma^3 m}}, \tag{3}$$

where $q$ is the electron charge, $n$ is the charge density, $\varepsilon_0$ is the permittivity of free space, and $\gamma^3 m$ is the relativistic longitudinal mass of the electron. Assuming a constant accelerating electric field of 85 MV/m, a final beam energy of 38 MeV, a beam length of 5 ps (1.5 mm), and a 250 $\mu$m radius, the plasma frequency and transit time were computed as a function of position. These parameters are similar to those seen in the experiment conducted at the Brookhaven SDL. The total number of plasma oscillations in the beam can be computed from $f_p t_r$, where the transit time $t_r = \int v_z^{-1} dz$, evaluated from $z=0$ to the $z$-coordinate at which the number of plasma oscillations is desired to be computed. In the case of maximum beam energy of 38 MeV, this corresponds to approximately 45 cm. Space charge effects can be neglected when the number of plasma oscillations is smaller than 1. The cumulative total number of plasma oscillations as a function of the $z$-coordinate for total charge between 1 pC and 1 nC is shown in Fig. 2. The number of plasma oscillations approaches 1 when the beam has a total charge of 5 pC. At the SDL deep ultraviolet (DUV)-FEL, beams with deep modulation densities at repetition rates between 0.5 and 1.6 THz could be generated with total charge varying between 20 and 200 pC. Based on the assumptions in Fig. 2, the experiment probes a transition region between space charge and emittance dominated regimes, where space charge effects play a role but might not destroy density modulation imposed at the cathode.

## II. DESCRIPTION AND SETUP OF THE DUV-FEL FACILITY

This experiment exploring electron beam density modulation used only parts of the DUV-FEL facility[22] with some slight modifications from typical usage. At the time of this

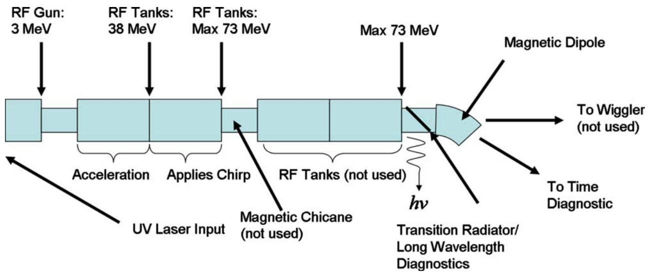

FIG. 3. (Color online) (Color Online) Block diagram of DUV-FEL facility.

experiment, the accelerator itself was based on a 1.6 cell S-band radio frequency photoinjector, an associated drive laser, and an accelerating linac comprised of four accelerating sections. The drive laser pulse was coded with terahertz modulations in order to serve as a switch at the photocathode. Since photoemission from copper is prompt (subfemtosecond),[23] the laser beam time profile will closely resemble the form of the resulting electron beam in the absence of space charge forces. The diagnostics at the DUV-FEL facility were used to measure the longitudinal phase space of the resultant electron beam after acceleration. A 2 cm aluminum mirror oriented at 45° was available for insertion into the beamline to generate backward transition radiation. This light is directed out of the beamline through a z-cut crystalline quartz window and measured with a single element bolometer. A block diagram of the facility setup used in this experiment is shown in Fig. 3. For this experiment, the laser input point, the time profile diagnostics, the transition radiator, and the long wavelength (terahertz) diagnostics are of primary interest.

## A. Drive laser

Generally, when this facility is used as a FEL, the frequency tripled Ti:sapphire drive laser produces a 5–10 ps long pulse at 266 nm. This generates an electron bunch of similar length after reaching the copper photocathode. The drive laser system exploits the high bandwidth inherent to the Ti:sapphire laser to generate a pulse of appropriate length and energy. In this case, a stretcher based on dispersion introduced by a diffraction grating lengthens the 100 fs pulse from the oscillator to ~200 ps. This allows the pulse to be amplified to a higher energy than might otherwise be possible since the extended pulse length keeps the energy density low. After amplification, the pulse is recompressed to the appropriate length for the application, in this case near 10 ps, at which point it can be efficiently converted to the third harmonic, 266 nm, a wavelength of sufficient energy to overcome the work function of copper. This type of amplification technique is generally referred to as a chirped-pulse amplification system.[24]

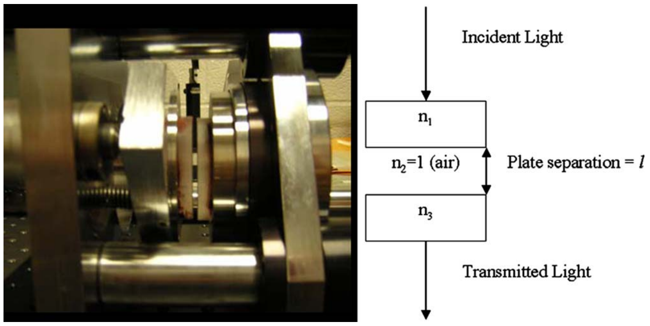

FIG. 4. (Color online) (Left) Photograph and (right) schematic model of Fabry–Pérot interferometer.

The method employed in this experiment to modulate the drive laser relies on the fact that the original 100 fs drive laser pulse is only partially recompressed, and after frequency tripling results in an ~5 ps pulse. This leaves a frequency correlation with time known as a chirp. A Fabry–Pérot interferometer (comb filter) is used after the laser is converted to the ultraviolet to remove some frequency components in a periodic way. Given the presence of the chirp, this generates a modulated laser pulse.

A photograph and simple model for the Fabry–Pérot interferometer is shown in Fig. 4. It is considered as a three-layer system, namely, two dielectric plates separated by an air gap.

The indices of refraction for the dielectric plates are set such that the proper reflectance and transmittance are achieved at each interface for a given wavelength. For this specific electron accelerator related application, the reflectance was chosen to be near 50%, as a compromise between finesse and transmitted energy. Typical analysis of a Fabry–Pérot system assumes that the incident pulse is cw, which is not appropriate in this case because the pulse length is on the order of the cavity spacing. Assuming normal incidence, the frequency dependent transmission coefficient can be calculated for the entire structure using the method of impedance transformation[25] and is given by

$$\tau(k_2)=\frac{2Z_3'(k_2)}{Z_3'(k_2)+Z_1}, \tag{4}$$

where $Z_m$ is the impedance of the $m$th region (assuming the relative permeability of the optical media is 1, $Z_m=Z_0/n_m$, where $Z_0$ is the impedance of free space and $n_m$ is the index of refraction of the optical media in the $m$th region), $k_m$ is $2\pi(\lambda_0/n_m)$ in the $m$th region, and $Z_3'$ is given by

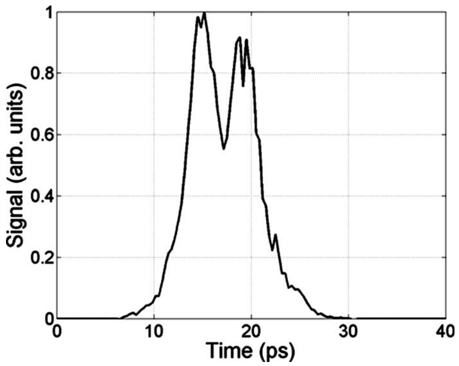

FIG. 5. Cross-correlation measurement of a typical unmodulated drive laser pulse intensity.

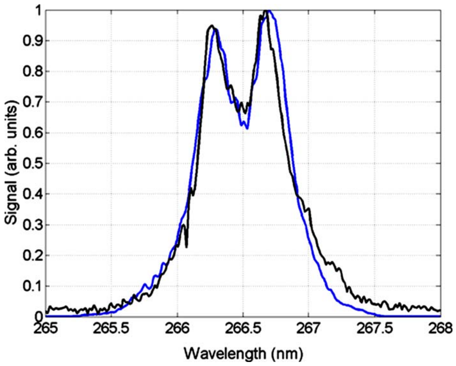

FIG. 6. (Color online) Input laser spectrum (blue) compared with calculation based on model (black).

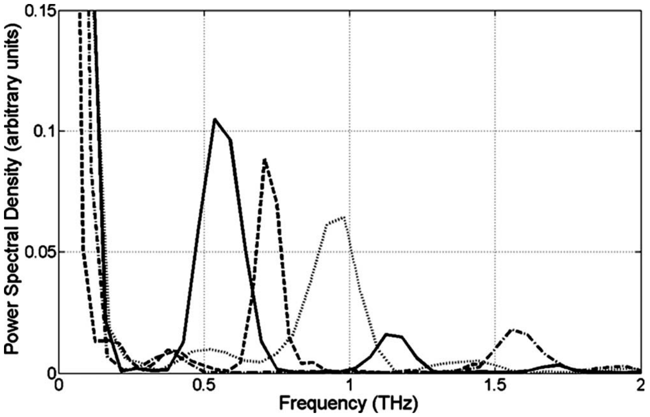

FIG. 8. Power spectral density of drive laser pulse for various Fabry–Pérot cavity spacings.

$$Z_3'(k_2) = Z_2\left(\frac{Z_3 \cos k_2 l + iZ_2 \sin k_2 l}{Z_2 \cos k_2 l + iZ_3 \sin k_2 l}\right), \tag{5}$$

where $l$ is the cavity spacing of the Fabry–Pérot interferometer. This transfer function, multiplied by the Fourier transform of the laser pulse, yields the output of the interferometer system. The laser pulse can be modeled with the following expression:[26]

$$E(t) = \frac{1}{\sigma\sqrt{2\pi}}\exp\left(\frac{-t^2}{2\sigma^2}\right)\exp(i\omega_0 t + i\beta t^2). \tag{6}$$

Equation (6) describes a pulse with a linear chirp that has a Gaussian envelope with standard deviation $\sigma$. The instantaneous frequency of this pulse is given by

$$\omega_i(t) = \frac{d\phi(t)}{dt} = \omega_0 + 2\beta t, \tag{7}$$

and so $\beta$ is the parameter that describes the linear chirp. Computing the Fourier transform of the laser pulse, multiplying by the transmission coefficient, and taking the inverse Fourier transform yields the electric field of the laser pulse as a function of time after emerging from the interferometer.

A scanning cross correlator[27] and a spectrometer were used to measure the laser pulse during the experiment. The scanning cross correlator gives the time profile of the laser beam with 250 fs resolution. A typical example of an unmodulated laser pulse is shown in Fig. 5 (although the pulse does not exhibit a smooth profile).

The chirp parameter for the model, $\beta$, was determined by minimizing the mean square error between the measured unmodulated laser pulse and the result of the model. Figure 6 compares the measured and modeled spectrum of this unmodulated pulse.

Inserting the Fabry–Pérot interferometer into the laser pulse generated a subpicosecond pulse train. Figure 7 shows the experimental and calculated intensities for two different pulse trains, with the cavity spacings estimated at 260 and 207 $\mu$m, respectively. In this case, the interferometer is operating in a "direct frequency to time" mode, where the spectrum looks similar to the time profile of the laser pulse as a result of the linear chirp.

It is clear from Fig. 7 that the frequency of the laser modulation can be tuned by changing the cavity spacing of the Fabry–Pérot interferometer. The power spectral density of the laser pulse gives a clear picture of the modulation frequency, and this is shown for various pulses in Fig. 8. This

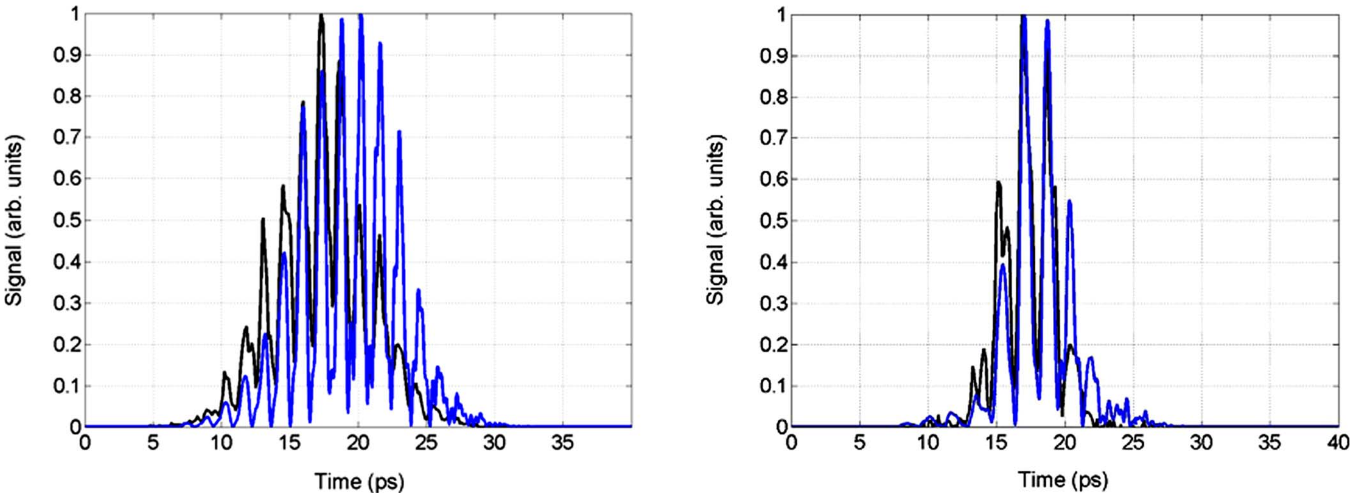

FIG. 7. (Color online) Cross-correlation measurement of modulated laser intensity (blue) compared with theory (black) for a cavity spacing of 260 $\mu$m (left) and 207 $\mu$m (right).

system was used to successfully modulate the laser pulse at frequencies between 0.5 and 1.6 THz.

The tunability and simplicity of the Fabry–Pérot system enabled a system well suited to creating a modulated electron beam in the linear accelerator. One convenient advantage that the Fabry–Pérot system offered over other modulation schemes, such as a pulse splitter-delay line combination, is that the output of the system depends mostly on the self-alignment of the interferometer mirrors rather than its alignment with respect to the rest of the laser system. While there is a $\cos(\theta)$ term that appears when the beam is not at normal incidence, this essentially changes the effective cavity spacing and does not cause the device to operate in an unacceptable way (it still produces laser modulation). While still requiring care, this made insertion and removal of this device into the laser system more convenient.

## B. Electron beam diagnostics

The accelerator diagnostics previously developed at the DUV-FEL are well suited to study of the longitudinal electron beam phase space. Preliminary experiments at this facility used an implementation of the rf zero-phasing technique to make longitudinal measurements.[28] In this case, an energy chirp that creates a correlation between time and energy is placed on the beam. This chirp is generated by using a rf accelerating section set at "zero-phase" relative to the electron beam, such that the head of the beam gains energy, while the tail of the beam loses energy (or vice versa). The beam is then passed through a spectrometer (magnetic dipole). The correlation between energy and time can be used to create a longitudinal electron beam profile measurement. However, depending on the phase space characteristics of the incident electron beam, the results of this measurement can be ambiguous. For example, two rf zero-phasing energy spectra are shown in Fig. 9. These measurements were made under significantly different circumstances. The beam in Fig. 9(a) has 200 pC total charge, is initially unmodulated, accelerated to 110 MeV, and compressed in a magnetic chicane prior to measurement. The beam in Fig. 9(b) is initially modulated by the drive laser switch, has 125 pC total charge, is accelerated to 73 MeV, and is not compressed in the magnetic chicane. It is interesting that the energy spectra look qualitatively similar; however, the actual structure shown in Fig. 9(a) has been shown to be dominated by energy modulation and caused by the longitudinal space charge instability,[4] while the structure in Fig. 9(b) is shown, by these experiments, to exhibit significant fluctuations in the electron beam density profile.

This ambiguity can be mitigated by measuring the entire longitudinal phase space; this can be done with tomographic reconstruction techniques.[29,30] This reconstruction is formed by taking several projections of the two dimensional longitudinal phase space. The projections are formed by placing an energy chirp on the beam, similar to the rf zero-phasing technique. Rather than being used at a single zero phase and a fixed amplitude, the phase of the second accelerating structure is varied about its crest phase to impart different amounts of chirp on the electron beam. In the case of these measurements, the beam was accelerated to 38 MeV in the first accelerating structure and up to 73 MeV at crest phase in the second. The projection of the longitudinal phase space onto the energy axis is accomplished with an electron spectrometer (magnetic dipole), located after the accelerating sections. The longitudinal phase space at the entrance of the second structure at 38 MeV can be recovered from these projections. A projection of the longitudinal phase space onto the position coordinate reveals the physical density distribution.

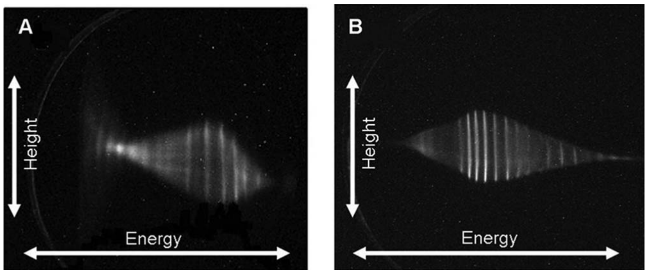

FIG. 9. (Left) rf zero-phase measurement of initially unmodulated compressed electron beam; (right) rf zero-phase measurement of deeply modulated uncompressed electron beam.

## C. Terahertz diagnostics

Any density modulation present on an electron beam will affect the nature of radiation it produces. If some mechanism causes a single electron to emit a specific wavelength of light, a bunch train of electrons separated by that wavelength would emit in such a way that their electric fields would add in phase. The result would be enhanced emission at that wavelength, with the resultant electric field proportional to the square of the number of electrons in the beam. If on the other hand, all of the electrons were randomly distributed throughout the beam, the electric fields would add incoherently, and the resultant electric field would be directly proportional to the number of electrons in the beam. The coherent emission could serve as a source of light, an electron beam diagnostic, or cause unwanted effects on the beam depending on the particular machine.

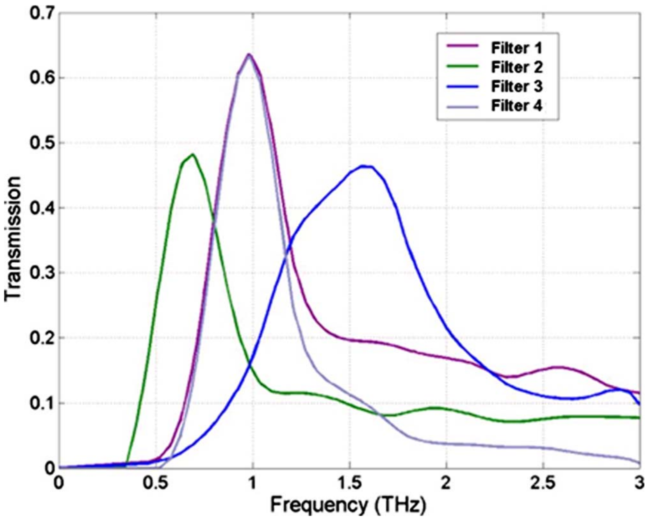

FIG. 10. (Color online) FTIR characterization of terahertz filters.

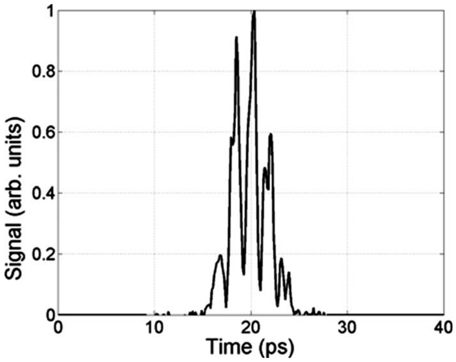

FIG. 11. Input laser intensity measured with cross correlation.

As described above a mirror can be inserted into the beam. CTR is expected to be observed from this mirror at terahertz wavelengths due to the modulation imposed on the electron beam. The CTR is detected by a single element bolometer that was equipped with several band-pass filters. Recording the amount of energy measured with each filter in place gives an idea of how much energy falls into each band from the modulated electron beam.

The design of the terahertz filters was based on ideas developed for microwave applications.[31] More recently, these types of filters were used for terahertz applications.[32] The filters are constructed from a perforated metal sheet, with either Cartesian or hexagonal symmetry. The finite thickness of the sheet results in the filter having resonance and waveguidelike characteristics. Light at wavelengths much smaller than the hole will transmit through the mesh, while light with large wavelengths will be reflected, resulting in a high pass filter. The frequency characteristics of these filters are dependent on the hole size, the spacing between the holes, and the thickness of the material. A reasonable model for this filter type is given by Chen,[31] and this model was used as a guide when purchasing materials. The filters were characterized on a Fourier transform infrared (FTIR) system, and the results are shown in Fig. 10.

The degree of correlation between the measurements and the theory is about the same as that seen by Winnewisser *et al.*[32] The peak transmissions of each of the filters are located at 0.703, 0.967, and 1.56 THz.

## III. RESULTS

The goal of this effort was to determine how a particular deep modulation imposed on an electron beam at the cathode is modified by forces experienced during the process of acceleration, including space charge. A combination of PARMELA[33] simulation results, electron beam tomographic reconstructions, and terahertz radiation measurements together form a picture of the electron beam dynamics in the parameter space of this work. The laser modulation frequency was tuned from 0.5 to 1.6 THz as described above, while the charge was varied experimentally between 20 and 200 pC. The PARMELA simulations explored much lower and higher charge levels as well. The general trends for the results hold for all settings of the modulation frequency; that is, increasing charge causes a reduction in the peak value of the form factor and also a reduction in the frequency at which the peak of the form factor is located. This behavior corresponds to debunching of the beam. The detailed results from one particular laser profile input, as shown in Fig. 11, are presented here.

The modulation peak of the laser profile in Fig. 11 is at 0.5 THz. PARMELA simulation results in Fig. 12 show the electron beam longitudinal density after acceleration to 38 MeV at the entrance to the second accelerating tank for 20 and 200 pC beam. These simulation results can be compared to experimental results based on the longitudinal phase space reconstructions, which represent state of the electron beam at the same location and energy.

It is clear from Fig. 12 that the modulation does not change much in the case of low charge, but in the case of high charge, almost all of the contrast in the density modulation is gone. The debunching can also be characterized by calculating the longitudinal form factor as a function of frequency and total charge, as shown in Fig. 13.

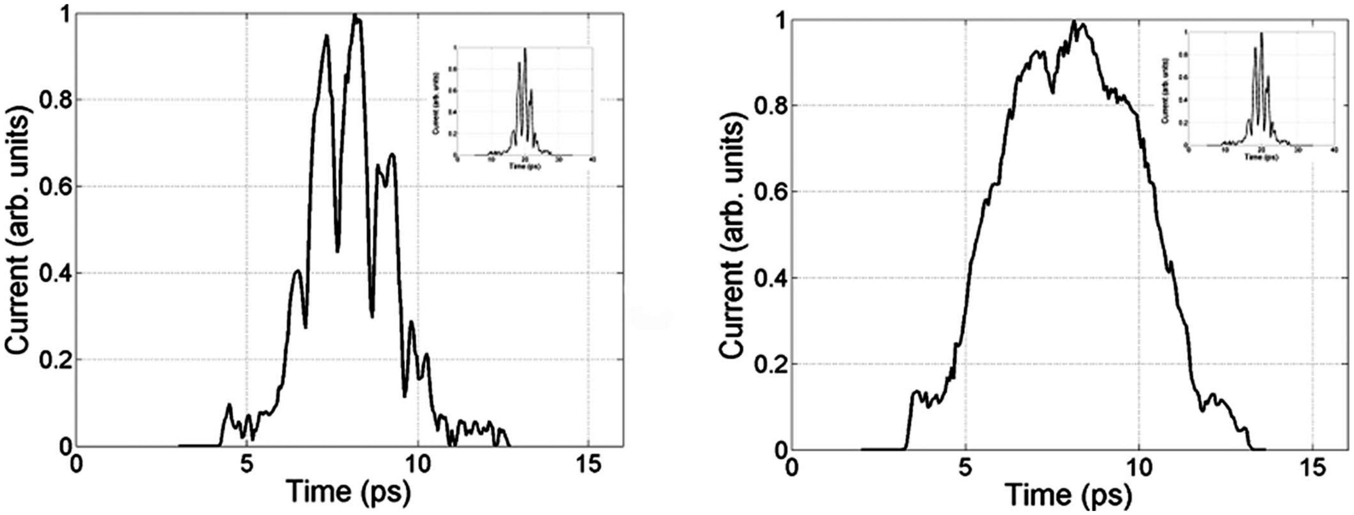

FIG. 12. (Left) Electron beam longitudinal profile for a 20 pC beam; (right) electron beam longitudinal profile for a 200 pC beam; (inset) initial laser pulse.

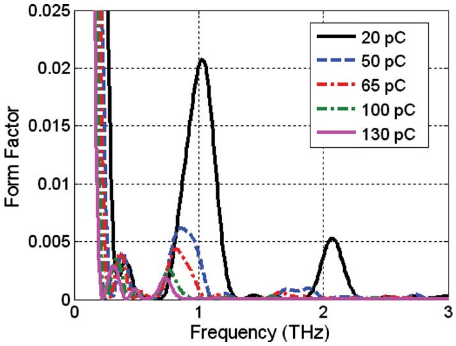

FIG. 13. (Color online) Form factor as a function of frequency and total charge.

It is interesting to note how the peak of the form factor falls, as well as the frequency of modulation at the peak of the form factor, as shown in Fig. 14. In Fig. 14, the frequency peak starts initially above that of the initial laser pulse due to the rf compression at the low charge levels;[34,35] this is consistent with results typically seen in this accelerator at the bunch charge used. However, as the amount of charge increases and space charge plays a larger role, this peak frequency drops below the initial modulation frequency of the laser. Figure 15 shows how the peak of the form factor varies as a function of the accelerator *z*-coordinate as well as total charge.

Figure 2 indicated that the plasma oscillations should slow as the beam is accelerated, and so it is not surprising that the falling form factor should be arrested after the beam reaches sufficient energy. The specific way in which the beam debunches is illuminated through the measurements made with the tomographic reconstruction technique. Examples of several longitudinal phase space reconstructions for total charge ranging between 20 and 200 pC, for the initial laser pulse shown in Fig. 11, are displayed in Fig. 16.

In Fig. 17, the projection of the longitudinal phase space onto the time coordinate is shown for a total bunch charge ranging from 20 to 200 pC. These results are compared with the PARMELA simulations, which maintain some qualitative agreement.

Washout of the density modulation occurs because the phase space of each electron bunch grows in both the longitudinal and energy coordinate, such that when projected onto the longitudinal coordinate, their ends overlap. The phase space of individual bunches appears to rotate as charge increases. It is interesting that each electron bunch remains separated by voids in the phase space while the separation in longitudinal density is reduced. As the bunch charge increases, the density modulation washes out further, and the angle of rotation in phase space of each bunch is increased.

The loss of density modulation does occur more quickly at higher laser frequency. Figure 18 shows a reconstruction of the longitudinal phase space, as well as a longitudinal density profile based on the phase space projection for a laser pulse with 1.6 THz initial modulation. While the density modulation has been somewhat washed out, the individual bunches are still fairly well defined in phase space. Even as the beam modulation washes out in density space, it is important to note that the longitudinal phase space of this beam is not approaching the phase space of a beam that is not prebunched. Figure 18 compares these two side by side. The distinction is important, as a prebunched beam may pass through an appropriate dispersive section, causing the electron bunches to rotate upright once more, allowing the density modulation to re-emerge and degrade beam quality as a result of a collective effect such as CSR. In fact, such a conversion between energy and density modulation has been demonstrated in simulation for an electron beam passing through a chicane compressor.[36] It is also interesting to note that the phase space reconstruction shown on the left side of Fig. 18 corresponds to the same electron beam that produced the rf zero-phasing profile shown in Fig. 9(b). It is clear that some density modulation remains on this electron beam, while the apparent modulation on the beam in Fig. 9(a) was shown to be dominated by energy fluctuations.

Although the details of the relationship between total charge and form factor are different for varying initial modulation frequency, the trends in the data are independent of this variation. However, to emphasize the point that tunable modulation was achieved, the form factors of the measured

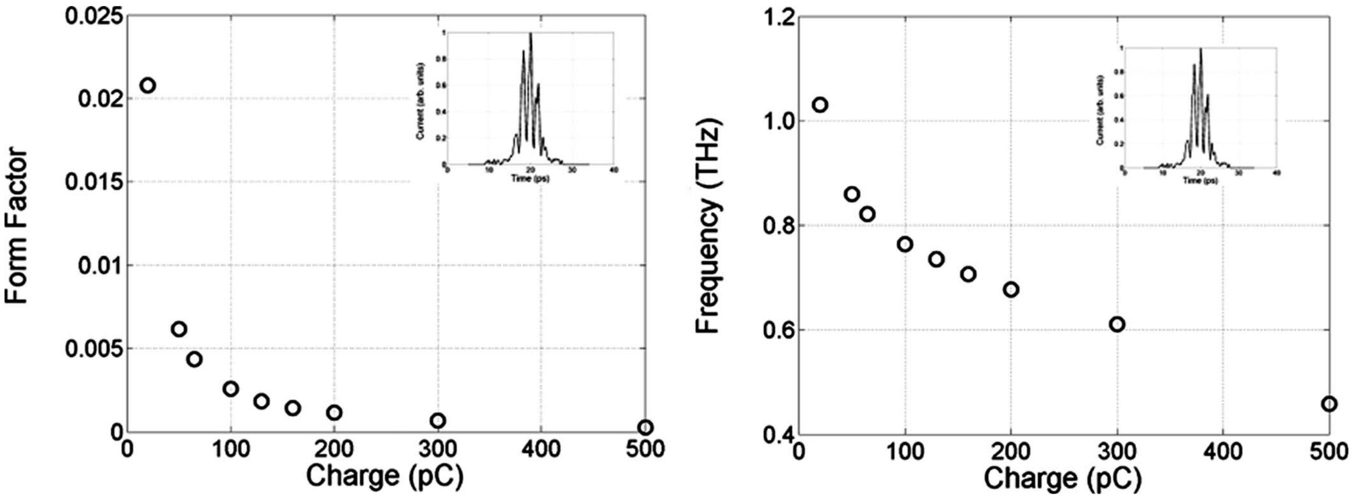

FIG. 14. (Left) Form factor peak as a function of charge; (right) frequency at which form factor peaks as a function of charge; (inset) initial laser pulse.

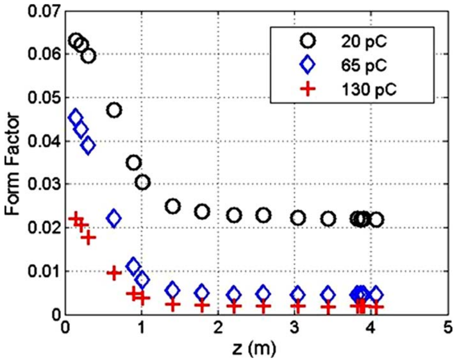

FIG. 15. (Color online) Peak form factor as a function of accelerator $z$-coordinate and total charge.

longitudinal density for three different cases are shown in Fig. 19. The peaks of these curves are at 0.7, 1.1, and 1.5 THz.

Terahertz radiation measurements also agree well with the behavior described so far. After acceleration, a mirror was inserted into the beamline at approximately 45° angle, which produces backward transition radiation which can escape from the accelerator through a diagnostic port. The terahertz light is transported to a single element bolometer that can detect the total incident terahertz energy. Since the frequency and total terahertz energy are dependent on the beam structure, this structure can be inferred by characterizing the terahertz light incident on the detector. Four different terahertz filters were used as described above. Filters 1–4 correspond to peak transmissions of 0.703, 0.967, 0.967 (with better out of band rejection), and 1.56 THz. The amount of radiation that would be incident on the detector can also be calculated in the following way:

$$W_{\mathrm{tot}} = \int\int\int (\sin\,\theta)(d\theta)(d\phi)(d\omega)\frac{d^2W_1}{d\omega d\Omega}[N_e + N_e(N_e - 1)f_L(\omega)f_T(\omega,\theta)]T_{\mathrm{air}}(\omega)T_{\mathrm{filt}}(\omega)T_{\mathrm{guide}}(\omega)T_{\mathrm{bend}}, \quad (8)$$

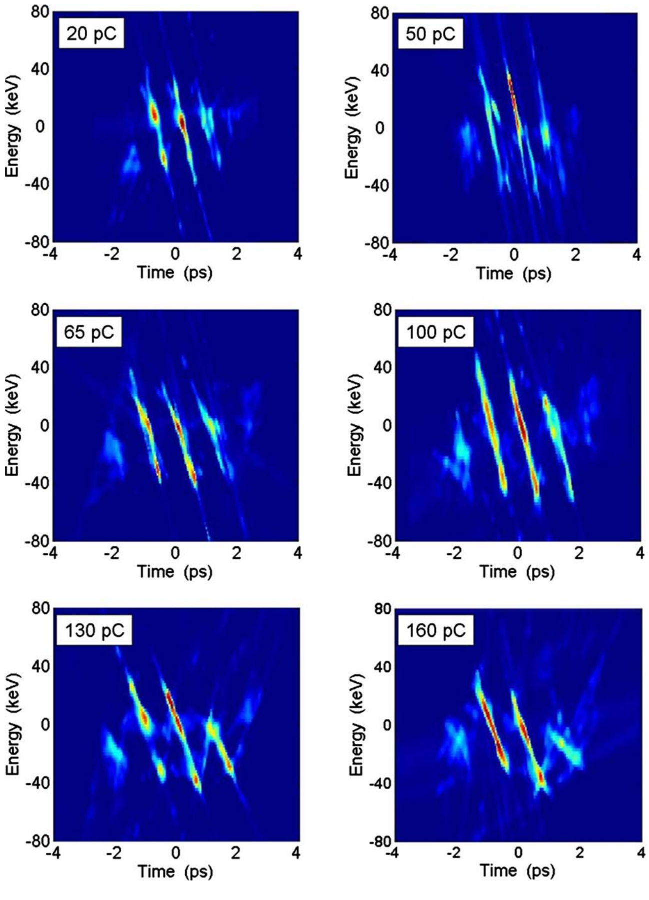

FIG. 16. (Color online) Longitudinal phase space reconstructions at various levels of total charge with a 0.5 THz input laser modulation.

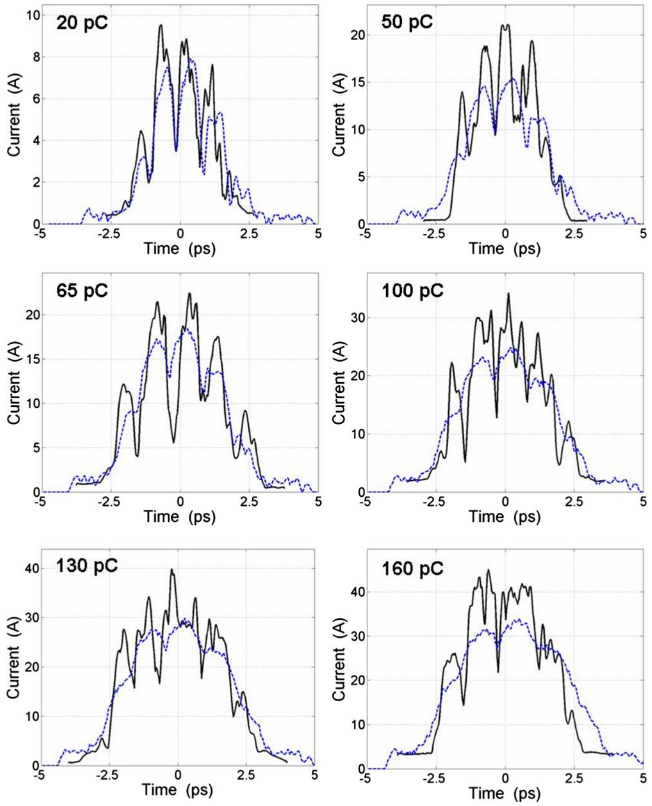

FIG. 17. (Color online) Projection of longitudinal phase space onto the time coordinate from experimental measurements (solid) and PARMELA simulations (dashed).

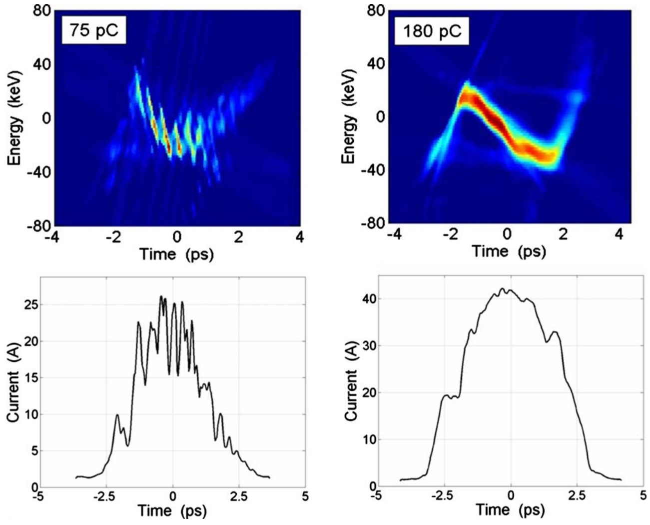

FIG. 18. (Color online) Phase space reconstructions (top) and respective longitudinal projections (bottom) of a beam prebunched at high frequency (left) and of an unmodulated beam (right).

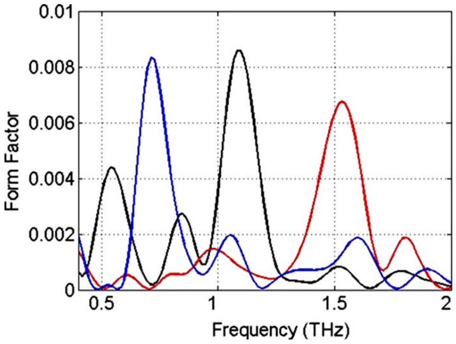

FIG. 19. (Color online) Electron beam form factor for three different initial laser modulation frequencies.

where the radiation from a single electron, $d^2W_1/d\omega d\Omega$, is modified by the longitudinal and transverse form factors, $f_l(\omega)$ and $f_t(\omega)$, the number of electrons in the bunch, $N_e$, the transmittance due to water absorption in the air, $T_{\text{air}}(\omega)$, the transmittance due to the waveguide, $T_{\text{guide}}(\omega)$, the measured transmittance due to the filters, $T_{\text{filt}}(\omega)$, and the transmittance due to the bends in the transport system, $T_{\text{bend}}$. $T_{\text{air}}(\omega)$ was estimated with atmospheric modeling software,[37] $T_{\text{guide}}(\omega)$ was estimated with simple waveguide attenuation calculations,[38] and $T_{\text{bend}}$ was estimated to be 0.4.[39] Finally, the radiated energy is integrated over the appropriate solid angle and the spectral range from dc to 3 THz (the cutoff at long wavelength is due to losses at the exit aperture, and this is taken into account in the radiation calculation from a single electron). The specifics for calculating the backward transition radiation from a single electron interacting with a finite size radiator at a 45° angle of incidence, which is the case for our experiment, are described well by Dobrovolsky and Shul'ga.[40] The main effect of the finite radiator is to produce a low frequency cutoff in the spectrum of the radiation. The results of this calculation for the electron beam profiles described above are compared to the actual bolometer measurements in Fig. 20. The blue data points with error bars represent experimental measurements taken directly from the bolometer. The black data points are generated by taking the electron beam profile from PARMELA and calculating the amount of terahertz light that should be measured at the detector based on Eq. (8).

The trends in Fig. 20 show good agreement between the calculated and measured results. The reason for the differences in energy level may be due to instrument calibration errors or errors in the estimation of the various parameters in Eq. (8). However, the general agreement between the calculated and measured results supports the notion that the emitted terahertz radiation is affected by the beam longitudinal structure in the manner previously described, and, while dependent on the charge density, which this structure survives acceleration from the cathode.

The PARMELA simulations also allow for exploration of electron beams with very low and very high total bunch charge. The laser profile input shown in Fig. 11 was used for simulations ranging from 10 fC to 1 nC. The peak of the form factor is determined over this entire range after beam acceleration and is shown in Fig. 21.

The result of the PARMELA simulations can also be used to calculate the total amount of terahertz radiation energy that would be generated and reach the bolometer when the total bunch charge varies between 10 fC and 1 nC. The results are shown in Fig. 22. Along with the simulation results, denoted by a diamond, terahertz calculations based on the tomographic reconstructions are marked with a cross, and the actual bolometer measurements are denoted with a circle. The dashed line is a reference that increases with the square of the charge. Typical experiments employing bunched beams measure radiation as a function of charge and one expects to see the relationship denoted by this dashed line if there is a feedback mechanism, such as in the FEL, to prevent debunching. This behavior is noted here at very low total charge levels. Below the single pico-Coloumb level, simulations do indicate an increase in terahertz light that varies with the square of the charge. The reason for this is that space charge forces are not strong enough to cause den-

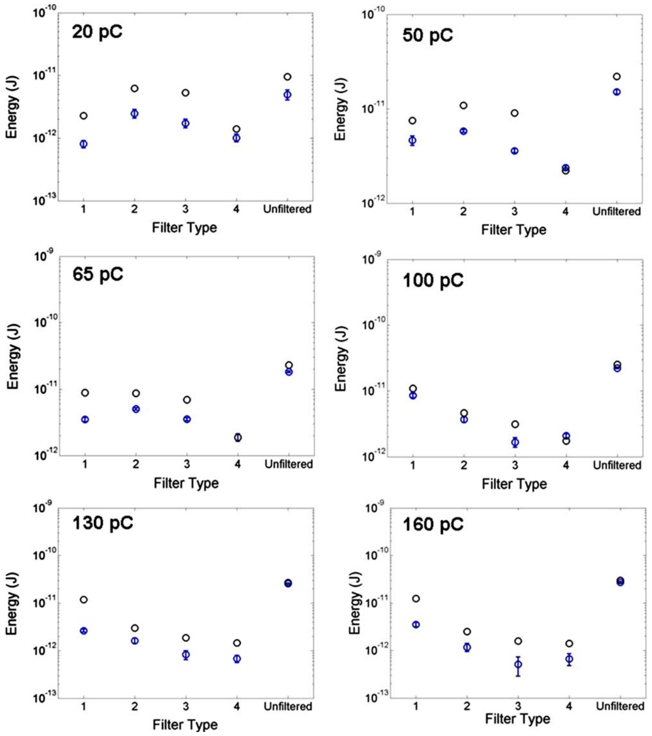

FIG. 20. (Color online) Comparison of measured terahertz radiation (with error bars) (blue) with calculations (black) as a function of filter type and total bunch charge.

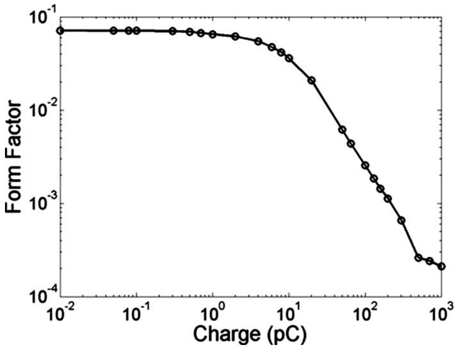

FIG. 21. PARMELA results showing peak form factor of a prebunched beam as a function of total bunch charge.

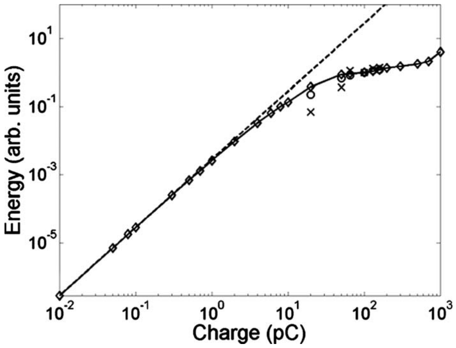

FIG. 22. Total terahertz energy incident on bolometer from simulation (diamond), calculation (cross), and actual bolometer measurement (circle).

sity washout. As the charge increases further, density washout begins to occur. This transition begins to occur on the order of a single pico-Coloumb, as anticipated by examining the plasma oscillations in Fig. 2. As charge increases, it is possible that the amount of terahertz light produced can actually decrease within a specific band. Eventually, the density washout will be nearly complete, and the total light produced will again increase, except only linearly with charge. This departure from the quadratic increase, as the beam transitions into a regime where space charge effects matter, is indicated by simulation as well as experiment and is also shown in Fig. 22.

## IV. CONCLUSION

Using the drive laser as a terahertz switch at the photocathode of a rf accelerator proved to be a useful way to produce a short bunch train with subpicosecond electron bunches. The results indicate that electron beam modulation is tunable in several ways: by changing the initial drive laser profile, by changing the injection phase in the accelerator (rf compression), and by adjusting the amount of charge in the beam. The tunable Fabry–Pérot system allowed for a variety of repetition frequencies to be employed, ranging from 0.5 to 1.6 THz. Tunable modulation of the electron beam appears to have been achieved experimentally between 700 GHz and 1.5 THz. At extremely low levels of charge (subpico-Coloumb), the space charge effects may be neglected and the beam maintains its bunch structure through acceleration to high energy. Above this level of total charge, space charge effects must be considered, and the density modulation on the electron beam begins to fill in. When this happens, each bunch tilts in phase space, which causes the projection into density space to exhibit washout. This washout becomes more pronounced as charge increases. Although the beam density profile becomes smoother as charge increases and the modulation fills in, the longitudinal energy-time phase space of such a beam is not similar to that of an unmodulated beam. The electron bunches remain separated by a void in phase space. A proper dispersive component (an instability such as that seen in the FEL to bunch an unmodulated beam is not required) could cause the individual bunches to rotate upright in phase space, thereby recovering the initial density modulation.

## ACKNOWLEDGMENTS

This work was carried out with the support from the U.S. Department of Energy, Division of Materials Sciences and Division of Chemical Sciences, under Contract No. DE-AC02-98CH10886, with the support from the Joint Technology Office, Office of Naval Research, and Army Research Laboratory, and with the support from Professor Chris Davis at the University of Maryland.

[1] J. G. Neumann, P G O'Shea, D Demske, W S Graves, B Sheehy, H Loos, and G L Carr, Nucl. Instrum. Methods Phys. Res. A **507**, 498 (2003).
[2] S. G. Biedron, J W. Lewellen, S. V. Milton, N. Gopalsami, J. F. Schneider, L. Skubal, Y. Li, M. Virgo, G. P. Gallerano, A. Doria, E. Giovenale, G. Messina, and I. P. Spassovsky, Proc. IEEE **95**, 1666 (2007).
[3] Z. Huang, M. Borland, P. Emma, J. Wu, C. Limborg, G. Stupakov, and J. Welch, Phys. Rev. ST Accel. Beams **7**, 074401 (2004).
[4] C. Limborg-Deprey and P. R. Bolton, Report No. SLAC-PUB-10941, 2004.
[5] K. Tian, R. A. Kishek, P. G. O'Shea, R. B. Fiorito, D. W. Feldman, and M. Reiser, Phys. Plasmas **15**, 056707 (2008).
[6] S. V. Benson, K. B. B. Beard, C. Behre, G. H. Biallas, J. Boyce, D. Douglas, H. F. Dylla, R. Evans, A. Grippo, J. Gubeli, D. Hardy, C. H. G. Hernandez-Garcia, K. Jordan, L. Merminga, G. Neil, J. Preble, M. D. Shinn, T. Siggins, H. Toyokawa, R. Walker, G. Williams, B. Yunn, and S. Zhang, Proceedings of the 2004 FEL Conference, 2004 , pp. 229–232.
[7] T. Shaftan and Z. Huang, Phys. Rev. ST Accel. Beams **7**, 080702 (2004).
[8] T. Shaftan, Z. Huang, L. Carr, A. Doyuran, W. S. Graves, C. Limborg, H. Loos, J. Rose, B. Sheehy, Z. Wu, and L. H. Yu, Nucl. Instrum. Methods Phys. Res. A **528**, 397 (2004).
[9] H. Loos, D. Dowell, S. Gilevich, C. Limborg-Deprey, Y. Shen, J. Murphy, B. Sheehy, T. Tsang, X. Wang, Z. Wu, L. Serafini, M. Boscolo, M. Ferrario, M. Petrarca, and C. Vicario, Proceedings of the 2005 Particle Accelerator Conference, Knoxville, TN, pp. 642–644.
[10] I. Bazarov, D. G. Ouzounov, B. M. Dunham, S. A. Belomestnykh, Y. Li, X. Liu, R. E. Meller, J. Sikora, C. K. Sinclair, F. W. Wise, and T. Miyajima, Phys. Rev. ST Accel. Beams **11**, 040702 (2008).
[11] J. R. Harris, J. G. Neumann, K. Tian, and P. G. O'Shea, Phys. Rev. E **76**, 026402 (2007).
[12] J. G. Neumann, J. R. Harris, B. Quinn, and P. G. O'Shea, Rev. Sci. Instrum. **76**, 033303 (2005).
[13] J. Harris, J. Neumann, and P. G. O'Shea. J. Appl. Phys. **99**, 093306 (2006).
[14] Y. Shen, T. Watanabe, D. A. Arena, C.-C. Kao, J. B. Murphy, T. Y. Tsang, X. J. Wang, and G. L. Carr, Phys. Rev. Lett. **99**, 043901 (2007).
[15] S. Nodvick and D. S. Saxon, Phys. Rev. **96**, 180 (1954).
[16] C. J. Hirschmugl, M. Sagurton, and G. P. Williams, Phys. Rev. A **44**, 1316 (1991).
[17] C. P. Neuman, W. S. Graves, and P. G. O'Shea, Phys. Rev. ST Accel. Beams **3**, 030701 (2000).
[18] J. Rosenzweig, G. Travish, and A. Tremaine, Nucl. Instrum. Methods Phys. Res. A **365**, 255 (1995).
[19] D. W. Rule, R. B. Fiorito, and W. D. Kimura, Proceedings of the Eighth Advance Accelerator Concepts Workshop, 1998.
[20] H. P. Freund, P. G. O'Shea, and J. Neumann, Nucl. Instrum. Methods Phys. Res. A **507**, 400 (2003).
[21] M. Reiser, *Theory and Design of Charged Particle Beams* (Wiley, New York, 1994).
[22] E. D.Johnson, I. Ben-Zvi, L. F. DiMauro, W. S. Graves, R. N. Heese, S. Krinsky, J. C. Sutherland, X. J. Wang, and L. H. Yu, Proc. SPIE **3925**, 26 (2000).
[23] T. Tsang, Appl. Phys. Lett. **63**, 871 (1993).
[24] S. Backus, C. G. Durfee III, M. M. Murnane, and H. C. Kapteyn, Rev. Sci. Instrum. **69**, 1207 (1998).
[25] C. Davis, *Lasers and Electro-Optics* (Cambridge University Press, Cambridge, 1996).
[26] A. Siegman, *Lasers* (University Science Books, Mill Valley, CA, 1986.
[27] H. Loos, G. L. Carr, A. Doyuran, W. S. Graves, E. D. Johnson, S. Krinsky, J. Rose, B. Sheehy, T. V. Shaftan, J. Skaritka, and L. H. Yu, Proceedings of the 2002 Advance Accelerator Concepts [AIP Conf. Proc. 647, 849 (2002)].
[28] D. X. Wang, G. A. Krafft, and C. K. Sinclair, Phys. Rev. E **57**, 2283 (1998).
[29] H. Loos, P. R. Bolton, J. E. Clendenin, D. H. Dowell, S. M. Gierman, C.

G. Limborg, J. F. Schmerge, T. V. Shaftan, and B. Sheehy, Nucl. Instrum. Methods Phys. Res. A **528**, 189 (2004).

[30] H. Loos, Nucl. Instrum. Methods Phys. Res. A **557**, 309 (2006).

[31] C. C. Chen, IEEE Trans. Microwave Theory Tech. **21**, 1 (1973).

[32] C. Winnewisser, F. Lewen, and H. Helm, Appl. Phys. A: Mater. Sci. Process. **66**, 593 (1998).

[33] J. Billen and L. Young. PARMELA, Report No. LA-UR-96-1835, 2000.

[34] P. Piot, L. Carr, W. S. Graves, and H. Loos, Phys. Rev. ST Accel. Beams **6**, 033503 (2003).

[35] P. G. O'Shea, S. C. Bender, B. E. Carlsten, J. W. Early, D. W. Feldman, A. H. Lumpkin, R. B. Feldman, J. C. Goldstein, K. F. McKenna, R. Martineau, E. J. Pitcher, M. J. Schmitt, W. E. Stein, M. D. Wilke, andT. J. Zaugg, Nucl. Instrum. Methods Phys. Res. A **331**, 62 (1993).

[36] D. C. Nguyen and B. E. Carlsten, Nucl. Instrum. Methods Phys. Res. A **375**, 597 (1996).

[37] D. Plusquellic, personal communication (29 November 2004).

[38] S. Ramo, J. Whinnery, and T. Van Duzer, *Fields and Waves in Communication Electronics* (Wiley, New York, 1965).

[39] G. L. Carr, personal communication (13 April 2004).

[40] S. N. Dobrovolsky and N. F. Shul'ga, Phys. At. Nucl. **64**, 994 (2001).